CHAPTER 3

DESIGNS AND MEASUREMENTS

This chapter presents the mechanical design and electrical circuits for the HRR TEA CO_2 laser, and basic measurements of their operational characteristics. The mechanical design includes the laser chamber, profiled electrodes, preionizer, fan array, heat exchanger, water cooling unit, vacuum and laser gas supply unit (Fig. 3.1). The electrical circuits consist of those of the low- (TTL) and medium- (SCR) for triggering, and preionizer- and main-discharge. The electric signals and performance of each circuit stage are also presented.

3.1 THE LASER CHAMBER

This system uses an integral laser gas chamber and wind tunnel gas recirculation design (hereafter called laser chamber) as shown in Figs. 3.1 and 3.2. Fig. 3.2 shows the physical dimension (in scale) of the laser chamber and mounting essemblies. This laser chamber was made from 1/8" thick mild steel joined by arc welding with two openings at the top and bottom for, respectively, the discharge electrode assembly, and loading of fan array and heat exchanger. Another two side-openings are located at the upper wind tunnel for back and front mirrors mounting respectively. The thickness and materials for the covering plates of these openings are illustrated in Fig. 3.2. Three 1/2" water-pipe standard sockets were used for gas inlet, gas outlet, and pressure gauges connections. This figure also illustrates the locations of the discharge spark gap and main and preionizer storage capacitors. All the vacuum sealing use 1/16" thick rubber gaskets (for the covering plates) and O-rings (for other mountings). The preionizer and fans

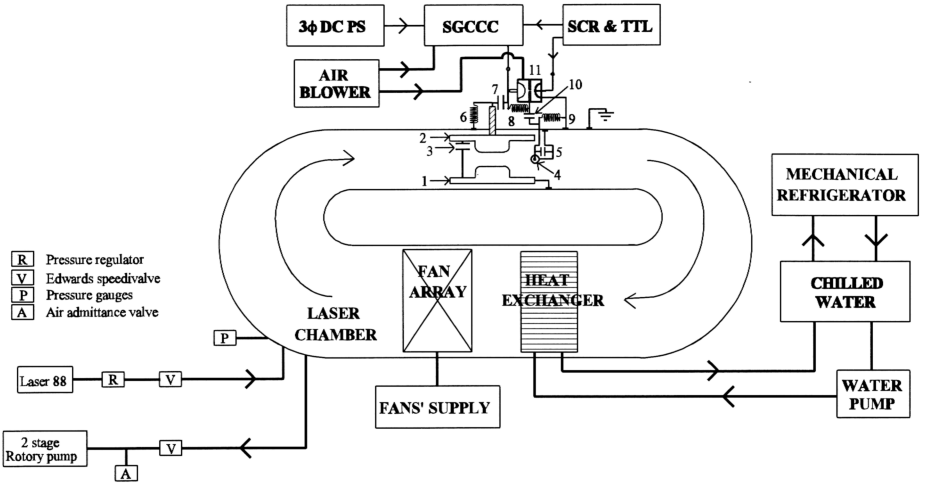

Fig. 3.1: General layout of the HHR TEA-CO_2 laser system.

The items are as follows : 3φ DC PS -- three phase DC power supply; SGCCC -- spark gap command charging circuit; SCR & TTL -- spark gap triggering circuits; 1 -- anode; 2 -- cathode; 3 -- main peaking capacitor; 4 -- coaxial UV-preionizer spark array; 5 -- preionizer peaking capacitor; 6 -- main by-pass inductor; 7 -- main storage capacitor; 8 -- preionizer charging inductor; 9 -- preionizer by-pass inducstor; 10 -- preionizer storage capacitor; 11 -- discharge spark gap. The anode is grounded firmly by seven thick copper wires (7/1.35mm core) to the grounded laser chamber.

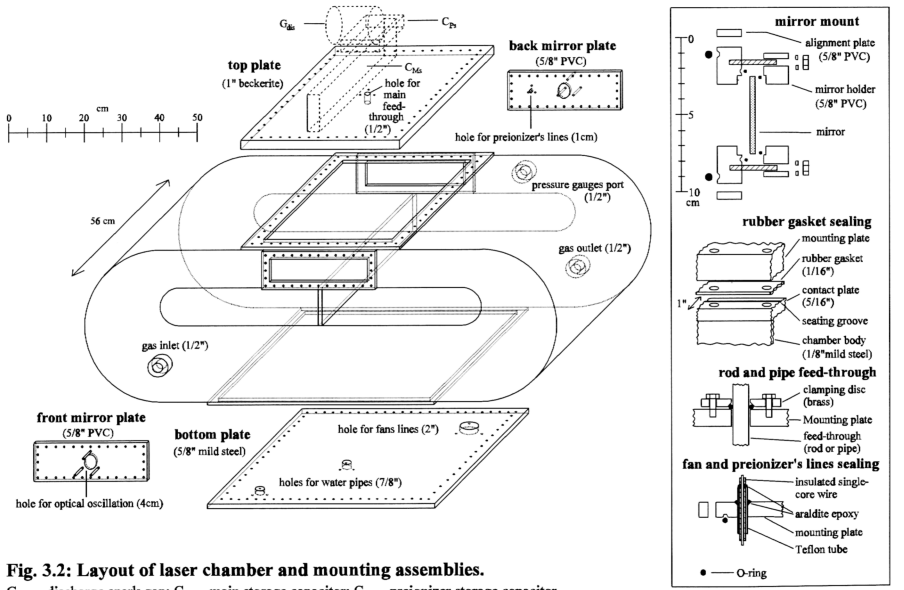

Fig. 3.2: Layout of laser chamber and mounting assemblies.

G_{dis} -- discharge spark gap; C_{Ms} -- main storage capacitor; C_{Ps} -- preionizer storage capacitor.

supply lines were sealed by araldite epoxy, as shown in Fig. 3.2. From the dimensions of this laser chamber, the chamber volume is approximately 214 liters without subtraction of the volumes of the inserted embodies inside the chamber.

A 2-stage rotary pump Edwards E2M5 with pumping capacity of 5.6 m^3/hour was used for evacuating the laser chamber through a 1/2" diameter, 1/2 m long rubber hose. Two Edwards speedivalves SP10K were used as the shutoff valves. The pressure gauges consist of Edwards CG3 - 25 mbar and 1000 mbar for indicating sufficient evacuation and gas filling pressure. Premixed industrial-grade gas mixture, Laser 88, with ratio of 8:8:84-CO_2:N_2:He at 1-atm was used for all the experiment.

The laser optics (oscillator) consists of a concave back mirror of 10-m radius of curvature, which is silver enhanced on gold coating on a silicon substrate. Its optical reflectivity is more than 99.7% at 10.6 μm. The output mirror is a plane, multilayer dielectric coated zinc selenide substrate with S_1 of 70% reflectivity and S_2 is anti-reflection at 10.6 μm. These two mirrors were arranged in the stable resonator configuration at 62 cm apart. Both mirrors are 2" in diameter and 5-mm in thickness and these were directly mounted to the laser chamber, as shown in Fig. 3.2. Mirror alignment is needed after evacuating and refilling of the laser chamber.

3.2 THE CHILLED WATER UNIT

The laser gas temperature rises during and after an electrical discharge. Previous work by Seow [77] using computer numerical calculations on TEA CO_2 laser model, showed that gas temperature rose about 400 ns after the onset of the electrical discharge, and then rose almost linearly during 700 to 2000 ns with a rate of about 30°C/μs. This delayed temperature-rise is due to the delay in the upper levels decay to the (01^10) level, and then vibrational-translational relaxing to ground, which is the main source of gas heating.

Dumanchin et al. [40] showed that the laser output energy increased linearly with the input energy with slope efficiency of 21% and temperature-rise was of the order of 75°C. This implies that the gas heating is not the limit to the output energy for single-pulse operation. However, accumulation of the discharge heated gas will increase the ambient gas temperature, during or after electrical discharge, to a level which can affect the laser output owing to the CO_2 levels relaxation times which change with temperature. This ambient temperature-rise can also affect the optical alignment by the thermal expansion of the laser chamber wall. These temperature effects have been observed experimentally by Dyer and Monk [50] and Baker et al. [48] by terminating the water flow to the heat exchanger. The former observed temperature-rise of ~45°C from ~57°C (output ~15 W dropped to ~7.5 W) while the latter obtained a temperature rise of ~42°C from ~40°C (output ~8.8 W dropped to ~7.8 W) in semi sealed-off operation. Therefore, gas cooling is needed for eliminating these temperature effects.

The heat removal unit for this laser is a 2-loop system: the mechanical refrigeration (chiller) loop and the chilled water loop. The mechanical refrigeration loop consists of an evaporator, a compressor, and an air-cooled condenser whereas the chilled water loop consists of a thermally insulated water tank, a water pump, and a heat exchanger. Fig. 3.3 shows the heat flow diagram from the laser head to the atmosphere outside the laboratory. The electrical power input is converted into heat and work (useful energy). Heat is carried by the laser gas while work is in form of radiation, i.e. the laser beam. There is also a small amount of heat generated by the fan array but this can be neglected. The laser gas is forced to pass through the heat exchanger by the fan array where gas-to-water heat transfer occurs. Normally, the fan array is installed at the downstream of the heat exchanger to prevent thermal damage by the hot laser gas. Since gas-to-liquid (water) heat transfer is involved or vice versa, a radiator type or tube-and-fin type is used with 8 fins/inch density which has dimensions of 52 cm long × 18 cm high × 8 cm thick. The

heat is carried away by circulating water. A water pump is used to force the water flow into the water tank located outside the laboratory. The water inside the tank is cooled by the evaporator where water-to-vapour heat transfer occurs through copper tube array. The vapour (refrigerant) is then compressed and forced to flow through the condenser (radiator type) by the compressor where the vapour is condensed by the cold atmospheric air and vapour/liquid-to-air heat transfer occurs. There is a considerable amount of heat introduced by the compressor, which is carried by the vapour after compression. Fans were used to force the atmospheric air flow through the condenser. There is also a small amount of heat loss from the gas chamber wall into the laboratory atmosphere.

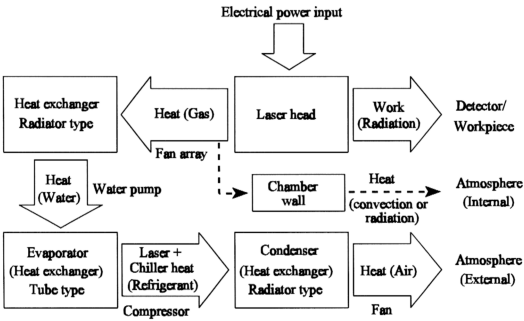

Fig. 3.3: The pattern of heat flow in the HRR TEA CO_2 laser heat removal system (Adapted from Rapp [91]).

The capacity of the chiller was measured by recording the water temperature drop with time inside the water tank when the chiller was on and laser was not operated and applying heat flow equation $Q_W = m_W c_W |T_{rW} - T_{iW}|$, where Q_W is the amount of heat flow, m_W the mass of water in the tank, c_W the specific heat capacity of water, and $|T_{rW} - T_{iW}|$ is the water temperature drop. The chiller capacity of ~10 kW at 4°C was found from the temperature drop vs time graph slope (rate of temperature drop) at 4°C.

3.3 FAN ARRAY AND GAS FLOW VELOCITIES

The fan array consists of a row of three axial flow fans (Oriental Motor MR18-DC, 200V/50Hz single phase, 45 W each, impeller diameter = 18 cm). From the static pressure vs air flow characteristics, the maximum rotation speed is ~2700 rpm with air flow capacity of ~5 m^3/min each at static pressure (S.P.) of ~4 mmAq (The maximum air flow at zero S.P. is 9.5 m^3/min each and the maximum S.P. at zero flow is 15.0 mmAq, and both have rotation speed of ~2600 rpm). The flow capacity is changed by changing the supply voltage with a variac.

The gas flow velocity was measured at a position 8 cm upstream from the center of the main electrode width by the pitot-static technique due to space limitation for locating the pitot tube. Since the flow velocity is much smaller than sonic, the laser gas can be treated as an incompressible fluid. Therefore, the flow velocity at the interelectrode gap can be calculated by a factor of β (the ratio of upstream to interelectrode flow cross-sectional areas) [11]. The flow cross-sectional area at the upstream position and at the interelectrode gap were measured to be about 9 cm × 55 cm and 1.15 cm × 43 cm respectively. There are buffer plates to prevent gas flow through other areas (both ends and top and bottom of the electrode assembly) besides that of the interelectrode gap. Therefore β is about 10 so that the interelectrode gap velocity is

$$v = \beta \times v' \approx 10v' \tag{3.1}$$

where v' is the upstream gas flow velocity.

Fig. 3.4 shows the upstream atmospheric air flow velocity distribution parallel to the length of the main electrode at a position 8 cm upstream from the center of the main electrode width. A pitot tube or probe (ALNOR 6060-12P, 1/2 inch diameter and 24 inches long) was used for velocity measurement which is governed by the following expression:

$$v = \sqrt{(2 \times \Delta P / \rho)} \tag{3.2}$$

where v is the measured gas velocity in m/s, ΔP the differential pressure generated by the pitot tube in Pa and ρ the flowing gas density in kg/m^3. At 70°F (~21°C) and 1 atm, density of air, CO_2, N_2, and He are 1.200, 1.835, 1.161, and 0.1657 kg/m^3. Therefore, 8:8:84-CO_2:N_2:He is 0.379 kg/m^3. The ΔP was measured by a differential pressure gauge (Dwyer series 2000 - Magnehelic 0-0.25" WC, the smallest scale is 0.005" WC).

Fig. 3.5 shows the interelectrode gas flow velocity as a function of the fans supply voltage in 8:8:84-CO_2:N_2:He at atmospheric pressure. These velocities were calculated based on Eq. 3.1 and each velocity is an average value of 4-v' values at positions z= 15, 24, 33, 44 cm from the laser chamber wall along the median plane of wind tunnel. Therefore, the fans supply voltage indicates the gas flow velocity. Note that, the interelectrode velocity profiles were not measured which may be higher at both ends of the laser channel.

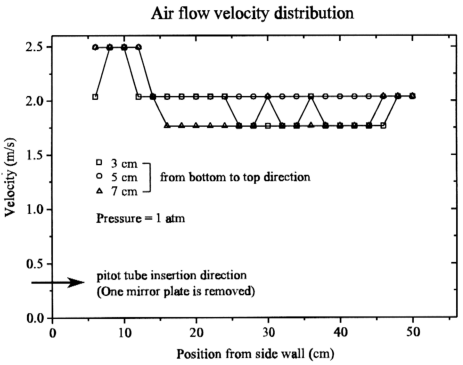

Fig. 3.4: Air flow velocity distribution parallel to the main electrode length and 8 cm upstream from the main electrode width center.

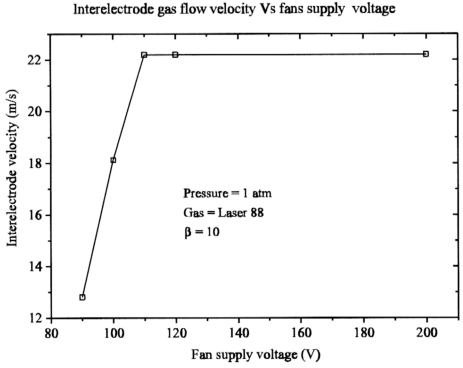

Fig. 3.5 Interelectrode gas flow velocity as a function of fans supply voltage. β value is as mentioned in text.

3.4 PROFILED ELECTRODE AND PREIONIZER

The profiled laser electrodes (Ernst, k = 0.03) are made from brass and have a center flat plane of about 1.8 cm width and the discharge is 43 cm long, as shown in Fig. 3.6. Four perspex rods (1" diameter, 3.6 cm long) were used to separate the top and bottom electrodes (Fig. 3.8). A single brass rod (1/2" diameter, 11 cm long) was used as the electrical feed-through. The average discharge width of this pair electrode, after a number of discharges, was found by the burn patterns on the anode and cathode, which have ~1.8 cm on anode and ~1.4 cm on cathode. Therefore, the discharge volume is approximately 80 cm ^{3}, ~1.15 cm (H) × ~1.6 cm (W) × ~43 cm (L).

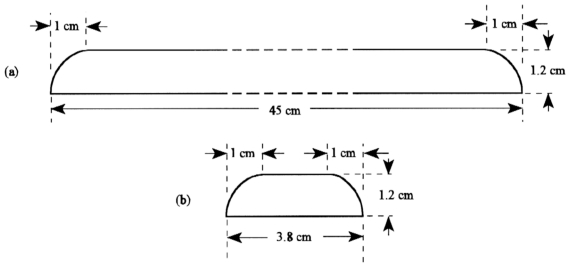

Fig. 3.6: The profiled electrode. (a) side view; (b) front view.

The UV-preionizer is a linear sliding-spark array, which is identical with the design of Ohwadano and Sekiguch [89], as shown in Fig. 3.7. This array is in coaxial configuration, which consists of an inner copper wire (as the current return path) inside a glass tube and 23-piece outer

trapezoid shaped stainless steel tube. Each gap has an initial separation of ~0.2 mm (total ~4.6 mm) but, after a number of discharges, the gap length increased to ~0.6 mm (total ~13.8 mm). The distance between the first gap to 23th (last) gap is 41.8 cm, which is about the length of the main discharge (~43 cm). This spark array was put in the median plane parallel to the main electrodes and 4.5 cm downstream from the main electrode width center. Preionizer positioned at upstream of the laser channel may affect the main discharge at HRR operation as mentioned by Tulip et al. [22]. Since the preionizer is in coaxial configuration and also has a closely parallel connected peaking capacitor (Fig. 3.8), the preionizer discharge is a fast and efficient UV source. Seguin et al. [90] found that high voltage, fast capacitor, and low inductance circuit would give a high current density (>30 kA/cm^2) resulting in an efficient production of UV light at 100-400 nm at high pressure (>100 torr) of He with CO_2 content.

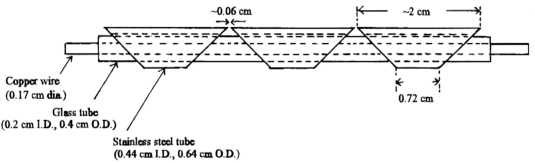

Fig. 3.7: Part of the coaxial configuration of the linear sliding-apark array UV-preionizer. Araldite epoxy was used for fixing shaped stainless steel tubes.

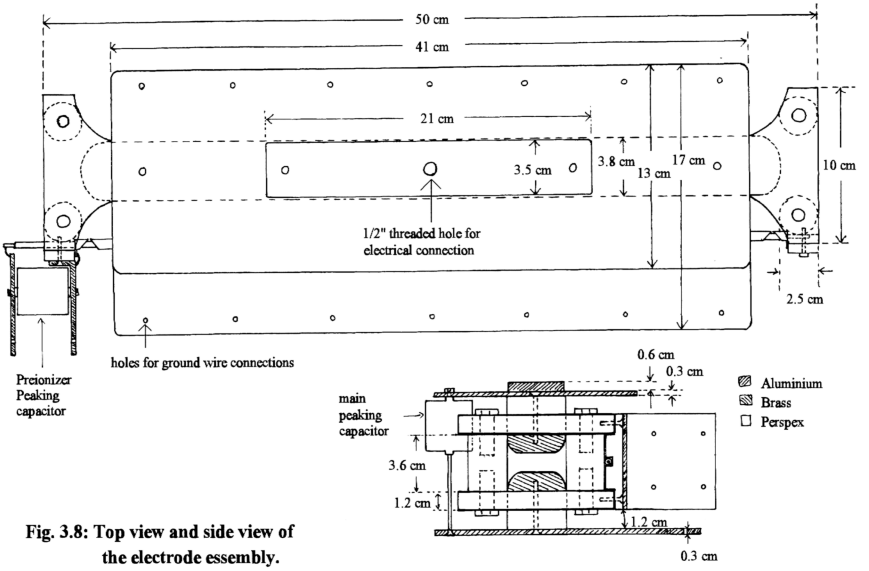

Fig. 3.8: Top view and side view of the electrode essembly.

3.5 OVERVIEW OF THE ELECTRICAL CIRCUIT

Fig. 3.9 shows a schematic/block diagram of the electrical arrangement for driving the HRR TEA CO_2 laser. The low voltage 555 timer unit generates two repetitively pulsed output (~3 V) to trigger SCR unit 1 (at t_0 and t_2) and SCR unit 2 (at t_1). Outputs (~250 V) of these two SCR units will feed to transformer 1 and transformer 2 producing open circuit output voltages of ~26 kV. Output from transformer 1 is used to overvolt a small steep-triggering spark gap in the steep-triggering circuit, which will trigger-overvolt the charging spark gap. Output from transformer 2 (negative pulse) is used to directly trigger a two-stage spark gap [37, 38], which will connect the preionizer circuit and the main circuit, after a delay of few hundreds nanoseconds. Since the two-stage spark gap has common ground cathode, the sign of the electrical pulses to preionizer and laser channel is negative.

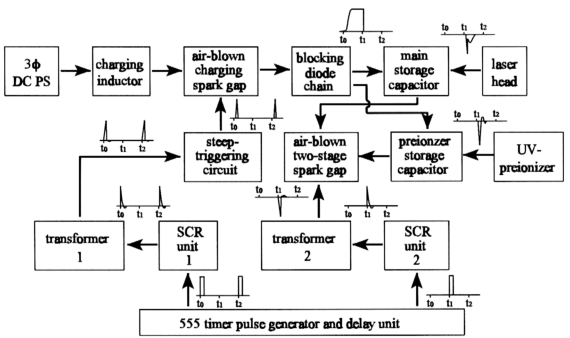

Fig. 3.9: Schematic diagram of the electrical flow in the HRR TEA CO_2 laser. The two-stage spark gap has common ground cathode.

A 3-phase, high-voltage, DC power supply (3ϕ DC PS) was used for charging the main and preionizer storage capacitors through charging inductor, charging spark gap, and blocking diode chain. Since charging only occurs when the charging spark gap is triggered, this charging method can be called as 'spark gap command charging'. An air blower (1.3 m^3/min at 300 mmAq static pressure) was used to improve the high-voltage recovery of the charging spark gap and the two-stage spark gap for HRR operation. A small aquarium air pump was used for flushing the steep-triggering spark gap.

3.6 HIGH-VOLTAGE POWER SUPPLY AND PROTECTION

The home-built high-voltage power supply consists of a 3ϕ variac (0-270 V/15 A output), a 3ϕ transformer (delta-to-wye, 10 kV/1A output), a 3ϕ full-wave H.V. rectifier built by series connected 1N5408 (3A, 1000 V) diode chains, and a smoothing capacitor (Maxwell, cat. no. 30640, 2 μF/25 kV). There is also a 1-A (F.S.D) DC ammeter and a H.V. kilovoltmeter built by resistor chain and 100-μA (F.S.D) DC microammeter. The power supply, electrical circuit elements (such as diode chains, charging inductor etc.), and spark gaps have to be protected. Fig. 3.10 shows the layout of the AC and DC or transient overload protection. AC overload is protected by the 15A fuses and DC or transient overload is protected by the 12 V relay, which is fed to the magnetic contactor circuit. The relay normally has a response time of the order of a few milliseconds. Therefore, the relay will cut off the supply to the contactor coil when a current pulse exceeds the preset value and last for more than the response time of the relay, activating the contactor to disconnect the 3ϕ input lines to the variac. The 8Ω relay shunt resistor is used because the relay is active at about 8 V supply to the coil.

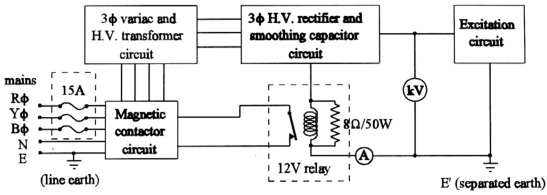

Fig. 3.10: AC and DC/transient overload protection.

3.7 555 TIMER AND SCR CIRCUITS

The 555 timer and SCR circuits were designed as shown in Figs. 3.11 and 3.12. This 555 timer circuit consists of four 555 timers (IC1-IC4). The pulse generator generates a square-pulse with three frequency ranges (1.6-45 HZ, 35-990 Hz, and 330-8900 Hz by switch S_1, 200 kΩ pot, and 2 MΩ pot) with duty cycle between 50% (low frequencies) to 52% (high frequencies). This output is used to trigger IC2 (falling edge) and IC3 (rising edge), which generate output pulse for triggering SCRs through twin-output pulse transformers. Pulse duration of ~6 μs (adjusted by 47 kΩ trimmer) is sufficient to trigger the SCRs in Fig. 3.12. The inverter is used for inverting the output signal of pulse generator so that IC3 is triggered at the rising edge of the pulse generator output (555 timer is only triggered by falling edges). Because the maximum duty cycle of the pulse generator output is 52%, the delay time of output IC2 with reference to output IC3 is 52% of the pulse generator output period. The tone burst generator is used to limit the pulse generator to one second duration when switch S_3 is closed and push button S_2 is pressed once. Therefore, one second burst pulses are generated, and single-pulse outputs can be achieved by setting pulse generator frequency to 1.6 Hz. The power supply to this 555 timer unit is shown in Fig. 3.12, which is a regulated 9V power supply. Figure 3.13 shows the electrical signals of

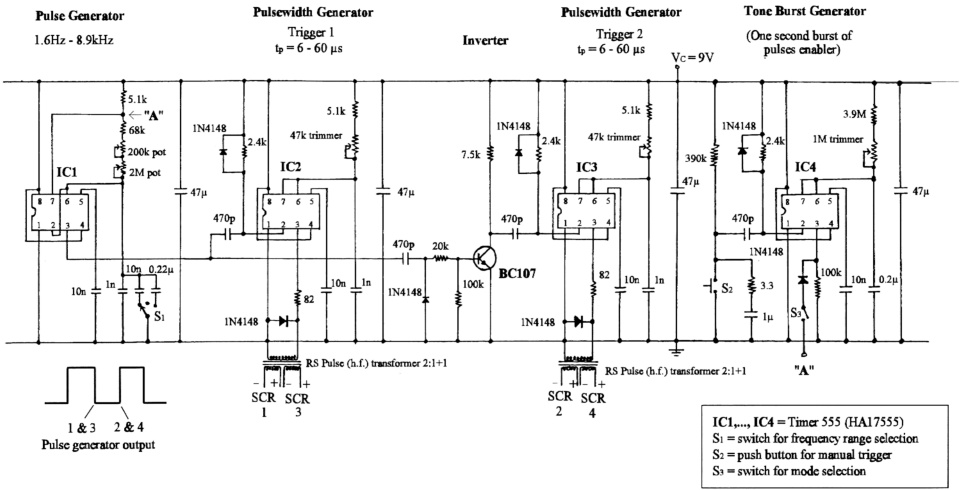

Fig. 3.11: Timer 555 pulse generator and delay circuit.

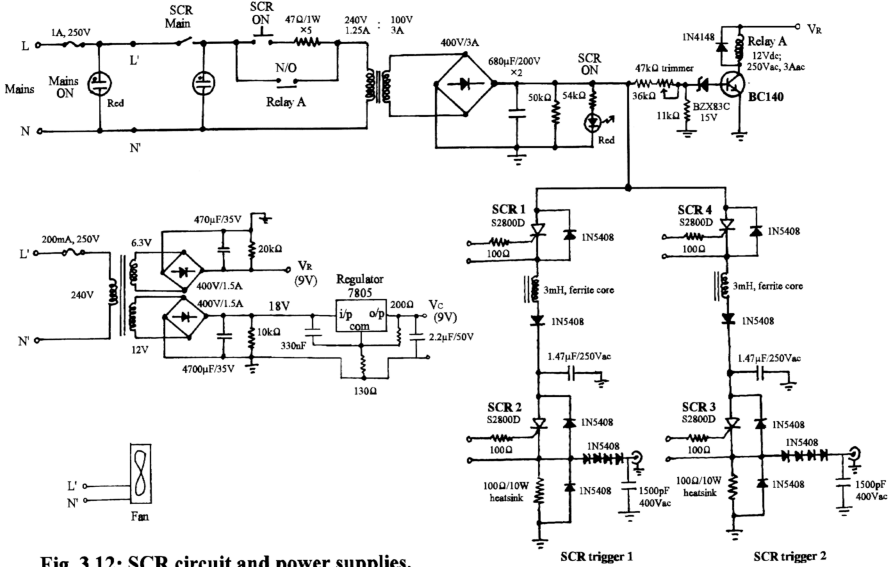

Fig. 3.12: SCR circuit and power supplies.

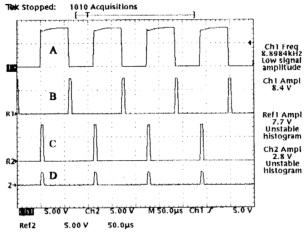

Fig. 3.13: The output electrical signals of the timer 555 circuit. The waveform labels represent as follow : A -- Pulse generator output; B -- IC2 output; C -- IC3 output; and D -- one of the secondary of the RS pulse transformer (2 : 1+1) outputs of IC3. The measured pulse generator positive duty cycle and the other waveforms pulse widths are 52.8% and 6.1-6.2 µs.

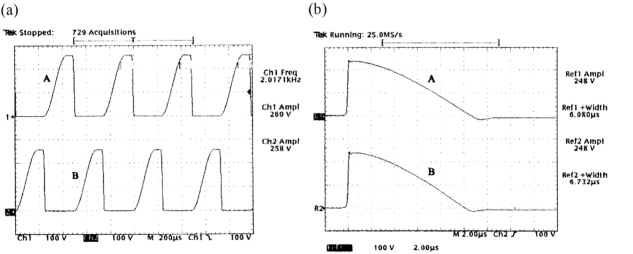

Fig. 3.14: (a) The storage capacitor voltage waveforms of SCRs. A -- trigger 2 and B -- trigger 1. (b) The output voltage waveforms of SCRs. A -- trigger 2 and B -- trigger 1. The operating PRF is 2017 Hz and SCRs outputs connected to the pulse transformers with completed following circuits (down to spark gap trigger pins).

the 555 timer circuit at frequency of 8.9 kHz.

The SCR circuit consists of two pairs of SCRs (Motorola S2800D, 400 V, 10 A, non-sensitive gate) to provide two outputs at HRR (Fig. 3.12). Within the SCR pair, one SCR is used as a command charging element and the other is used as a discharging element. It is because the holding current and circuit commutated turnoff times of these SCRs are normally a few tens of milliamperes and ~25 μs. Neither resistive charging nor inductive charging would be able to operate at HRR mode. SCR1 and SCR 3 are triggered simultaneously by the output of the IC2 circuit and, then the SCR2 and SCR4 are triggered after a delay of approximately half of the period between pulses (1/frequency). The charging inductors are made from a 1.5-cm diameter and 5 cm long ferrite core wound with SWG30 insulated copper wire. With these inductors, the maximum voltage across the 1.47 μF storage capacitor is almost double (~1.9) that of the supply voltage (smoothing capacitor, 680 μF × 2, voltage) and the blocking diodes are used to prevent charge flow back to the smoothing capacitor.

The 1N5408 diodes and 1500 pF output capacitors are used for protecting the SCRs from the feedback of the spark gap breakdowns. The SCRs and other circuit elements are also protected from overloading by the relay A circuit when SCRs are noise-triggered. The relay A will disconnect the mains to the power supply when the voltage across the 11 kΩ resistor falls below 15 V (Zener diode switches off). Furthermore, this protection circuit is also used to limit the DC voltage of the smoothing capacitor to the preset value (~130 V). Below this value, it will switch off the power supply.

This SCR circuit has been operated up to 2200 Hz but, when the charging inductors are replaced with 1 mH (saturable), frequency up to ~5000 Hz was achieved, which is limited by the storage capacitors charging times. Fig. 3.14 shows the storage capacitors voltage and SCRs output voltage. It has been found that the smoothing capacitor and storage capacitor voltage

decrease linearly with frequency from 150 V to 137 V and 278 V to 258 V when frequency increases from 1.6 Hz to 2000 Hz due to the power supply transformer regulation. Therefore, the output pulse amplitude also decreases with frequency.

3.8 THE HIGH-VOLTAGE CIRCUIT

The high-voltage circuit for operating this HRR TEA CO_2 laser was designed, as shown in Fig. 3.15. This circuit consists of

(a) charging inductors and their suppression circuit,

(b) charging spark gap and its triggering circuit and suppression circuit,

(c) blocking diode chain, and

(d) two-stage discharge spark gap and its main and preionizer circuits.

It is noted that all the individual circuit grounds are connected to the same point for minimizing the intercircuit interactions. There are some conditions for selecting the inductors L_{ch1}, L_{ch2}, L_{Mb}, L_{Pc}, and L_{Pb}.

(i) $L_{ch1} + L_{ch2} \gg L_{Mb}$ or $L_{Pc} + L_{Pb}$ in order the capacitor charging time is $\tau = \pi\sqrt{(L_{eq}C_{eq})}$, where $L_{eq} \approx L_{ch1} + L_{ch2}$ and $C_{eq} = C_{Ms} + C_{Ps}$.

(ii) A single layer inductor L_{ch2} was added in case of L_{ch1} interlayer insulator failure. If L_{ch2} is not added and both L_{ch1} and spark gaps fail, there will be a large discharge current from the main smoothing capacitor. This will generate high amplitude noise, which may damage the measuring instruments and circuit elements.

(iii) L_{Pb}, L_{Pc}, and L_{Mb} must be big enough in order to allow little current flow through them during operation times. The conditions are $L_{Pb}C_{Ps} \gg$ the preionizer discharge time, $L_{Pc}(C_{Ms}//C_{Mp}) \gg$ the time delay of first-to-second stage gap breakdown, and $L_{Mb}C_{Ms} \gg$ the main circuit discharge time, where $C_{Ms}//C_{Mp}$ is the parallel equivalent value.

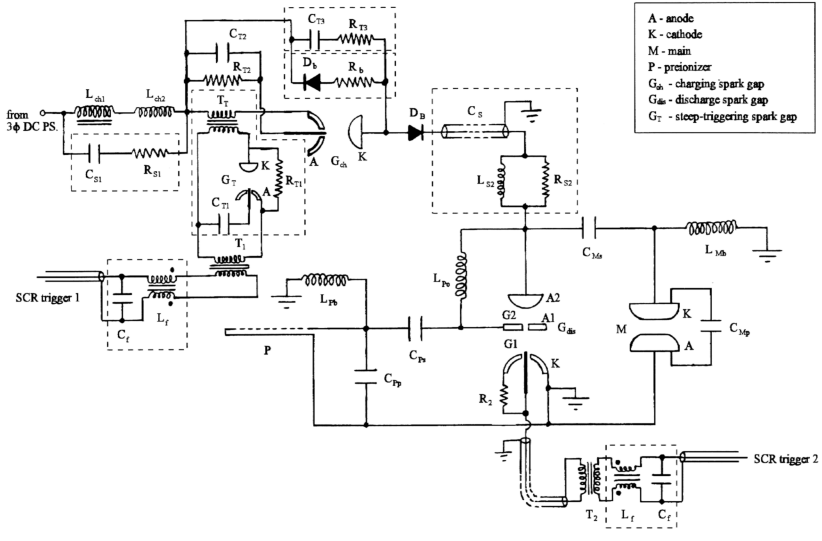

Fig. 3.15: High-voltage circuit for HRR TEA CO_2 laser.

The values and notations of circuit elements are given in table 3.1.

Table 3.1: List of notations and values for high-voltage circuit elements.

Symbol	Value	Name/Description
C_{Ms}	12 - 65 nF	main storage capacitor[a]
C_{Mp}	1.76 - 3.96 nF	main peaking capacitor[a]
C_{Ps}	2 - 10 nF	preionizer storage capacitor[a]
C_{Pp}	1.74 - 8 nF	preionizer peaking capacitor[a]
L_{ch1}	100mH, 1Adc	laminated iron core charging inductor
L_{ch2}	2.4mH	single layer charging inductor[b]
L_{Mb}	160μH	main by-pass inductor[b]
L_{Pc}	2.8mH	preionizer charging inductor[b]
L_{Pb}	220μH	preionizer by-pass inductor[b]
		spark gap triggering transformers for
T_1	1 : ~ 70	G_{ch} : primary - SWG21, secondary - SWG35
T_2	(250μH : 1.54H)	G_{dis} : modified TV transformer
D_B	30kV, 3A	H.V. blocking diode chain , 30 of 1N5408 in series
		damping/suppression circuit elements (charging)
C_{S1}	0.22nF	2 of 0.44nF in series[a]
R_{S1}	20kΩ	5 of 5kΩ/50W in series, wirewound type
		damping/suppression circuit elements (discharging)
C_S	100pF	1 m coaxial cable RG213/U
L_{S2}	1.1mH	charging by-pass inductor[b]
R_{S2}	1kΩ	5 of 5kΩ/50W in parallel, wirewound type
		back-flow circuit elements
D_b	30kV, 1A	30 of 1N4007 in series
R_b	5kΩ	5kΩ/50W, wirewound type
		trigger pins biasing resistors
R_{T2}	165kΩ	5 of 33kΩ/3W in series, carbon film type
R_2	1MΩ	2 of 510kΩ/1W in series , carbon film type
		steep-triggering circuit elements
C_{T1}	0.44nF	steep-triggering capacitor[a]
R_{T1}	1MΩ	2 of 510kΩ/1W in series, carbon film type
T_T	1 : 2.8	steep-triggering transformer, primary - RG-58/U coaxial
	(380μH : 2.9mH)	cable without braid and sheath, secondary - RS E.H.T. cable (25kVdc)
C_{T2}	10pF	trigger pin coupling capacitor, 10 cm RG213/U
C_{T3}	50pF	trigger pulse coupling elements, 50 cm RG213/U
R_{T3}	56Ω	56Ω/10W, wirewound type
		high frequency blocking filter elements (low-pass filter)
L_f	~10 μH each	1:1 single layer ferrite core, SWG 21
C_f	1nF	6kV, Z5V disc ceramic

[a] Murata ceramic doorknob capacitor (N4700 series) - 0.44, 1.3 and 2 nF / 40kV. A Maxwell plastic case pulse discharge capacitor (model no. 31552) , 25nF/50kV/25nH is also used in C_{Ms}.

[b] Single layer air core insulated copper wire with SWG 21 wound on PVC pipe. RG-213/U coaxial cable - 50Ω, 100pF/m

3.8.1 Spark Gaps Design

Fig. 3.16 shows the physical dimension of the design of the air-blown spark gap [35, 36]. The action of the blowing air is identical as the transverse gas flow in a HRR TEA CO_2 laser, which removes the residue discharge gas before the next pulse. However, the expansion of the heated air is larger than that of the TEA CO_2 laser discharge since the input energy density is larger and temperature rise is higher. Furthermore, the expansion is radial, which is different from that of the TEA CO_2 laser discharge guided by the pair electrode. An air sharing valve was used to divide the air flow in order that both spark gaps can operate at HRR mode. Since the discharge spark gap is operated at the normal trigatron triggering mode, the effect of the air blowing is more important. A small amount of the air is thus blown across the trigger gap in order to clean the discharge air.

3.8.2 Low-Pass Filter and Pulse Transformers

The low-pass filter consists of a capacitor C_f and a 1:1 ferrite core transformer L_f. Since the high frequency noise generated by the spark breakdowns are much higher than those of the trigger signal, design of this filter is simple. It was found that high frequency noise was almost completely suppressed by this filter with considerably small attenuation (~40 V) and neglected waveform distortion of the triggering signal.

Fig. 3.17 shows the constructions of the triggering transformer and the steep-triggering transformer. The TV transformer was modified by rewinding the primary. Since the secondary of the steep-triggering transformer is connected to DC high voltage, the RS E.H.T. cable was used for winding this secondary. Fig. 3.18 shows the primary and secondary voltages of the triggering pulse transformers at open-circuit. The rise time (10% to 90%) of this open-circuit output is ~4 μs. It was found that the open-circuit output decreased with frequency from 27 kV

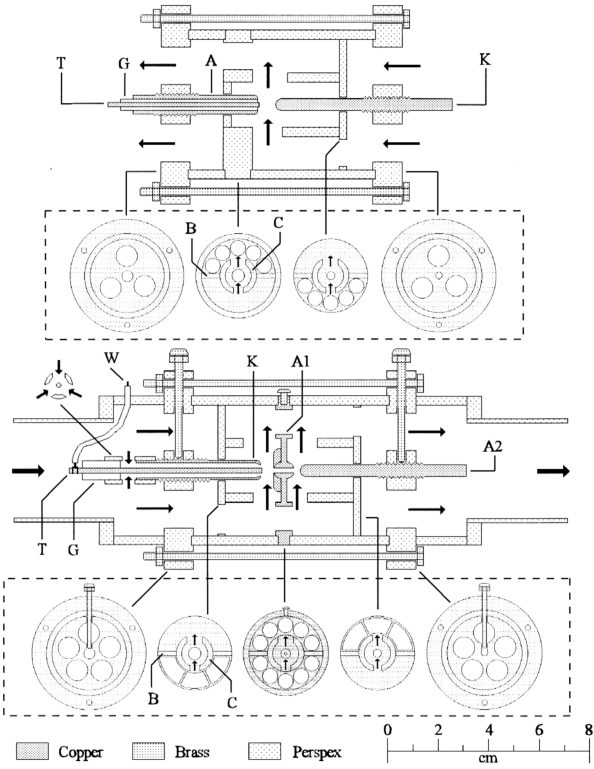

Fig. 3.16: Layout of the charging spark gap (upper) and the two-stage discharge spark gap (lower).

The components are as follows : A -- anode; A1 -- first stage anode; A2 -- second stage anode; B -- chamber dividing plates; C -- machined perspex tube;G -- glass tube; K -- cathode; T -- trigger pin; W -- trigger pin connecting wire. Arrows indicate the directions of air flow.

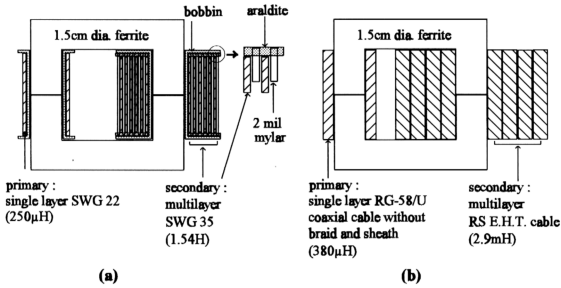

Fig. 3.17: The constructions of the pulse transformers. (a) triggering transformer T_1 and (b) steep-triggering transformer T_T. The modified TV transformer T_2 also has the same values as (a).

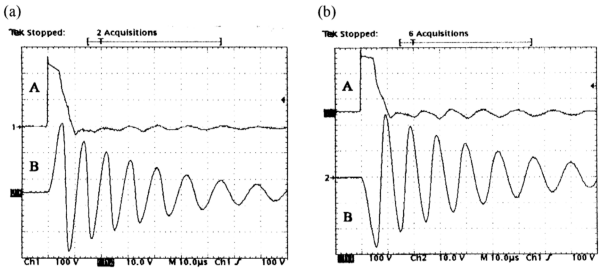

Fig. 3.18: Electrical signals of triggering transformers primary (A in 100 V/div) and secondary (B in 10 kV/div) voltage waveforms at open-circuit. (a) the transformer 1 and (b) the transformer 2 (modified TV transformer).

to 25.6 kV when frequency increases from 1.6 Hz to 2200 Hz. This was because of the decrease of the SCRs power supply voltage (150V to 137V) and the small increase in the voltage gain (the ratio of the peak output voltage to the peak input voltage) from 122 to 126. Note that the voltage gain is almost double (~1.8) of the calculated value by the step-up ratio (Table 3.1). This means that the undermatched condition occurs, which will cause the secondary to swing to almost double of the calculated value. The characteristics of the steep-triggering transformer will be given in the next section.

3.8.3 Steep-Triggering Circuit

This circuit consists of a capacitor C_{T1}, a small spark gap G_T, and a pulse transformer T_T, as shown previously in Fig. 3.15. Fig. 3.19 shows the construction of the steep-triggering spark gap G_T. Additional circuit elements R_{T1}, C_{T2}, R_{T2}, C_{T3}, and R_{T3} are needed in order that the circuit can function properly. The capacitor C_{T1} is charged up by the transformer T_1 through the trigger gap of G_T. At the same time, the trigger gap spark illuminates the main gap of G_T. When the C_{T1} reaches the main gap breakdown voltage of G_T (~7 kV), C_{T1} will discharge through G_T and T_T. The output of T_T will overvolt the trigger gap of G_{ch} and charge up the C_{T2}. At the same time, then the spark of the trigger gap will illuminate or photoionize the main gap of G_{ch}. Causing that the main gap to break down. Current flow back to the transformer negative leg through C_{T3} and R_{T3}. The resistor R_{T1} is used for discharging the C_{T1} and biasing of the gap G_T whereas R_{T2} is used for discharging C_{T2} and biasing of the trigger gap of G_{ch}. The R_b-D_b path is treated as the path for D_b reverse bias. Fig. 3.20 shows the electrical signals of the steep-triggering circuit operation. It was found that the breakdown of G_T depends on the frequency, which decreases with the increase of frequency. The gap distance of G_{dis} should be adjusted to the corresponding minimum trigger voltage (at maximum frequency) in order that the G_{dis} could operate over a large frequency range. Both the G_T and G_{dis} are operated in the trigger-overvolt mode.

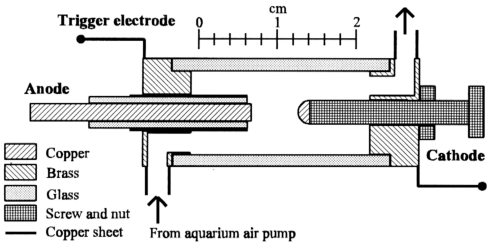

Fig. 3.19: Physical dimensions of the steep-triggering spark gap. Araldite epoxy was used for joining parts.

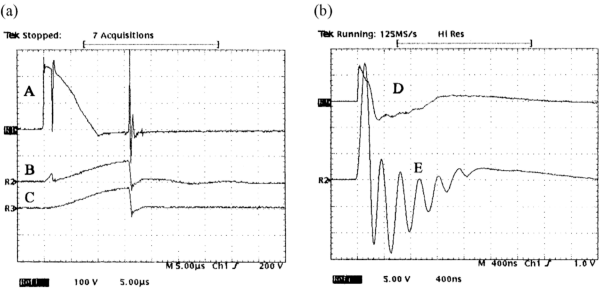

Fig. 3.20: Voltage waveforms in the steep-triggering circuit. (a) A and B -- transformer T_1 primary (100 V/div) and secondary (10 kV/div) and C -- C_{T1} positive terminal (time base is 5 µs/div). (b) D and E -- primary and secondary of T_T with secondary is open-circuited with risetimes of 6.8ns and 75ns respectively (time base is 400 ns/div).

3.8.4 Suppression of Electrical Oscillations

A parallel connected LR section was often used to damp (suppress) the voltage or current oscillations due to stray capacitances and inductances. Figure 3.21 shows a representative circuit for circuit analysis. For L » L_S, there are three conditions of the C_S discharge, i.e.

underdamped oscillation discharge, $\alpha > 1/2$ (3.3)

non-oscillation critically damped discharge, $\alpha = 1/2$ (3.4)

non-oscillation overdamped discharge, $\alpha < 1/2$ (3.5)

where $\alpha = R/\sqrt{(L/C_S)}$. Since L and R are in parallel, there must be current flow through L even when α « 1/2 resulting in voltage across C_S to swing over the zero voltage level. The critical condition is normally used for suppressing circuit current oscillations.

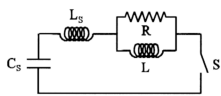

Fig. 3.21: Damping of circuit current oscillation. C_S and L_S are the circuit stray capacitance and inductance, R and L the insertion LR section, and S the representative switching element.

The suppression circuit C_S-L_{S2}-R_{S2} in Fig. 3.15 was used to overcome the voltage swing on the cathode of the G_{dh} when discharge spark gap G_{dis} breaks down. Voltage swing on cathode can cause overvolt breakdown in the G_{dh}. The inserted C_S was used for circuit calculation. Power

dissipation for R_{S2} is about $0.5C_S V_S^2 f$ where V_C is the main or preionizer capacitors charging voltage and f is the operating frequency. Figure 3.22 shows the voltage waveforms on the cathode of G_{ch} with different R_{S2} values.

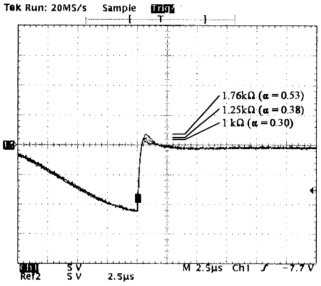

Fig. 3.22: Damping of C_{ch} cathode voltage swing by suppression circuit C_S-L_{S2}-R_{S2}. Triggering signal was used to charge up the C_S and G_{dis} gap was adjusted. The C_{Ms} and C_{Ps} were disconnected from G_{dis}. Vertical scale is 5 kV/div.

The R_{S1} value on the charging inductors (L_{ch1} and L_{ch2}) is difficult to be estimated since the winding capacitance of L_{ch1} is not known as shown in Fig. 3.23. Furthermore, the stray capacitance after the charging inductor L_{ch2} is also difficult to measure. Experiments showed that 20 kΩ resistance would give reasonable suppression as shown in Fig. 3.25. The capacitor C_{S1} was used as a blocking element during the charging cycle and as a shorted path for suppression after charging cycle was terminated. This value must be larger than the stray capacitance. Since C_{S1} was charged to V_0 during the charging cycle and discharged to 0 V after charging cycle, the power dissipation of R_{S1} is $C_{S1}V_0^2 f$ where V_0 is the power supply voltage. By this suppression

technique, the charging inductor insulator failure due to overheating or high voltage oscillation stress will be reduced.

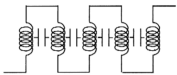

Fig. 3.23: Stray capacitors in a 5-layer windings inductor.

3.8.5 Spark Gaps Performances

(a) Voltage Multiplying Factor

The voltage multiplying factor is defined as

$$F_v = V_C/V_0 \tag{3.6}$$

where V_C is the storage capacitors voltage and V_0 is the power supply voltage. Figure 3.24 shows the effect of the air flow on voltage multiplying factor. Both curves have small F_v at low supply voltage, which saturate at high supply voltage. The saturation value (~1.75) is typical for this circuit at any gap separation. The electrode surface conditions can affect this F_v value which is increased by a small factor (~0.05) if the electrode surfaces are cleaned. Figure 3.25 shows the voltage drop across the charging spark gap. This figure shows a bigger voltage drop when the blower is on or when the current is smaller (at the beginning and ending of the charging cycle). The small peak at the ending portion of the charging cycle is due to the spark gap suddenly increasing in resistance, resulting in a faster anode-voltage rise time. Therefore the F_v is lower

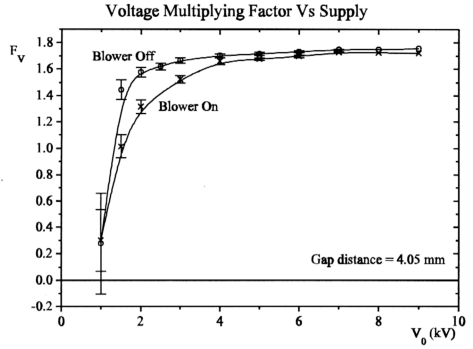

Fig. 3.24: Effect of the air flow on the voltage multiplying factor.

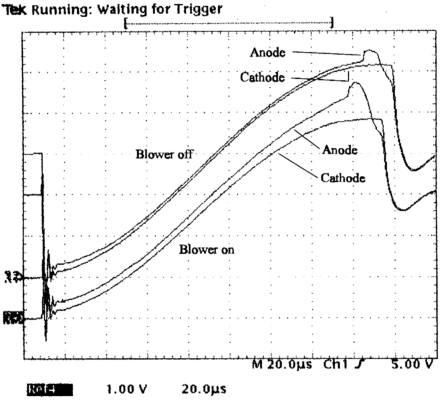

Fig. 3.25: Voltage drop across the charging spark gap. The gap distance is 2.25 mm and the power supply voltage is 3 kV. Note that the charging time is shorter for blower on because conduction terminated earlier.

than the typical inductive charging circuit (>1.9). In addition, this peak fluctuates in amplitude at low voltage range, resulting in F_v fluctuation. For a given supply voltage, the gap should be adjusted to give a small F_v fluctuation.

(b) Voltage Operating Range

Figures 3.26 and 3.27 show the voltage operating range of the charging spark gap and discharge spark gap (A single-phase H.V. power supply was used). These operating ranges will be used as guides in the adjustment of gap for different operating voltages. Note that ΔV_0 of discharge spark gap decreases with gap distance, which is due to $V_{0,\,min}$ which increases faster than the $V_{0,\,max}$. This means that a higher electric field is needed for trigger-breakdown when the gap distance increases and the corona production limits the $V_{0,\,max}$ rise with distance. The operating range is smaller than Craggs' due to small electrode diameters, which give higher field intensity on the electrode surface. An increase in the electrode diameter or changing of the insulator (perspex) should give higher $V_{0,\,max}$ value.

There is no test on the voltage operating range with respect to frequency because of frequently tripping of the power supply when spark gaps fail to recover. However, $V_{0,\,max}$, $V_{0,\,min}$, and ΔV_0 decrease with frequency [36, p. 184]. The $V_{0,\,max}$ and $V_{0,\,min}$ also slowly decrease with operating time (or number of pulses) with about constant ΔV [35, p. 125].

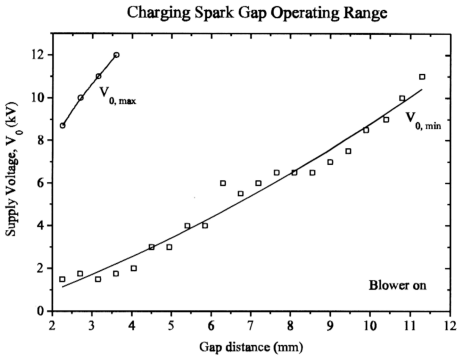

Fig. 3.26: The operating voltage of charging spark gap as a function of breakdown gap distance. $V_{0,max}$ is the maximum V_0 for gap self-breakdown with >1/s, which is greater than the time for resistive charging (R = 1.2 MΩ and C = 24 nF) and $V_{0,min}$ is the minimum V_0 for triggered breakdown with at least 10 shots sequence. The self-breakdown level is affected by the previous discharge.

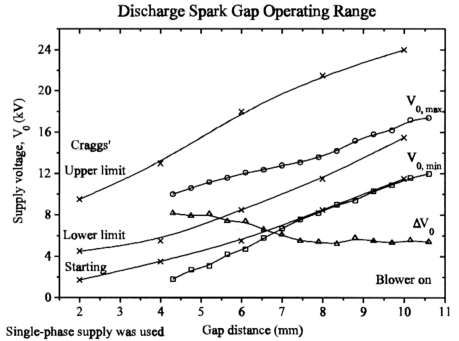

Fig. 3.27: The operating voltage of two-stage discharge spark gap as a fucntion of breakdown gap distance. The lower limit is the voltage where spark gap firing jitter < 0.2 μs (From Craggs [36]).

(c) Frequency Achievement

This main circuit was tested with dummy loads (Nichrome wire) of 12.4 Ω and 1.9 Ω for the preionizer circuit. Fig. 3.28 shows the storage capacitors voltage operating at ~2 kHz. Beyond this frequency, the spark gap failed to recover because of too short the recovery time for the charging spark gap. Therefore, the storage capacitors charging time limits the maximum operating frequency. No further test on higher voltages at high frequency due to the dissipating limitation of the dummy loads (~600 W).

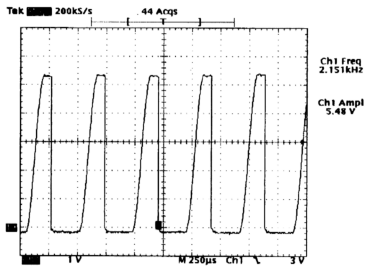

Fig. 3.28: Storage capacitors voltage waveform with C_{Ms} = 20 nF and C_{Ps} = 4 nF. Note that the flat top duration is about 70 µs.